buildings

Article

Experimental and Numerical Investigation of Plastic–Concrete Waterproof Walls of an Underground Granary Subject to Combined Bending Moment and Water Pressure

Hao Zhang, Kaiyi Han, Jinping Yang * and Lei Chen

School of Civil Engineering, Henan University of Technology, Zhengzhou 450001, China; zzbright@163.com (H.Z.); 2020920390@stu.haut.edu.cn (K.H.); chenleihe2008@163.com (L.C.)
* Correspondence: jping_yang@haut.edu.cn; Tel.: +86-0371-67758681

Abstract: To investigate the mechanical properties of plastic–concrete silo walls in practice, the mechanical properties and failure mechanism under the combined bending moment and water pressure were analyzed through the uniform loading test, water pressure test, and numerical analysis. The influence of the connecting plate spacing, radius, and the waterproof plate thickness on the water pressure-bearing capacity were analyzed. The test results show that the chemical adhesive force exists between the waterproof plate and concrete and can resist 20 kPa. The displacement and strain of the waterproof plate increases significantly with the increment in water pressure. When the water pressure reached 85 kPa, the specimen was damaged due to shear failure. The established numerical model was validated by the test results. The numerical analysis results show that the specimen failure mainly depends on the bolt strength when the thickness of the waterproof plate is greater than 14 mm or the radius of the connecting plate is greater than 60 mm. The relation between the design parameters and the water pressure-bearing capacity was proposed. Compared with the waterproof plate thickness, the connecting plate spacing and radius have greater influence on the water pressure-bearing capacity.

Keywords: underground granary; plastic-concrete wall; uniform loading test; water pressure test; numerical analysis

Citation: Zhang, H.; Han, K.; Yang, J.; Chen, L. Experimental and Numerical Investigation of Plastic–Concrete Waterproof Walls of an Underground Granary Subject to Combined Bending Moment and Water Pressure. *Buildings* **2022**, *12*, 893. https://doi.org/10.3390/buildings12070893

Academic Editors: Hongyuan Fang, Baosong Ma, Qunfang Hu, Xin Feng, Niannian Wang, Cong Zeng and Hongfang Lu

Received: 28 May 2022
Accepted: 20 June 2022
Published: 24 June 2022

1. Introduction

Underground granaries have a long application history in China [1]. Because they are built underground, they have the advantages of airtightness, low temperature, low storage cost, no requirement for fumigation, avoidance of pollution, etc. [2,3]. Compared with above-ground granaries, they also have the advantages of requiring less space, being concealed, and preventing fires [4,5]. In recent years, many scholars have devoted themselves to the study of new underground granaries, among which large diameter reinforced concrete underground granaries have become representative of modern underground granaries, and are notable for their achievements [6].

Concrete structures are widely used in engineering, and have the advantages of good modularity, integrity, and durability [7–10]. Similarly, the cast-in-place reinforced concrete underground silo is also an attractive structural form of the underground silo [11]. However, the issue of ensuring these silos are waterproof and moisture-proof still restricts their extensive application and promotion [12,13]. Polypropylene plastic is waterproof, corrosion-resistant, easy to construct, non-toxic and harmless [14], and meets food storage standards. In [15], the authors presented a plastic–concrete waterproof system with polypropylene plastic (PP) as the lining material. The waterproof system integrated the construction of the structure and ensured it was waterproof, and solved the problems associated with the difficulty in repairing the waterproof roll material and coating construction in the reinforced concrete structure. However, in order to ensure the safety of plastic–concrete silos, it is still necessary to carry out a composite stress analysis of the bending moment and water pressure on the silo wall. This has not been proposed in previous studies, e.g., ref. [15].

In order to improve the water resistance and durability of cast-in-place reinforced concrete underground silos from the perspective of applied science [16–19], and to improve the quality of internal grain storage, improving silo performance from the perspective of concrete materials is a popular research topic. Poonyakan et al. [20] improved low thermal conductivity concrete using plastic wastes. Kromoser et al. [21] proposed a novel thin-walled CFRP-reinforced UHPC beam based on second-generation implants. Flores-Johnson et al. [22] presented fiber-reinforced foamed concrete with a shaking table test. Al-Fakih et al. [23] studied the rubberized concrete through numerical analysis; however, only the vertical loading was considered. Lee et al. [24] theoretically proposed thin-walled UHPC flanges. Kozłowski et al. [25] studied the shear behavior of AAC masonry unit walls. These studies indicate that, in order to more accurately obtain the material properties of concrete structures, it is necessary to conduct model tests [26–28].

In addition, it is also necessary to fully study the static characteristics of cast-in-place reinforced concrete underground silos prior to their designing [29–31]. Static properties include tensile, compression, bending, and shear properties [32–34]. Mastering these static characteristics is required to ensure the safety of the designed underground bunker [35,36]. More complex stress modes, such as simultaneous compression and bending, are also lacking research. In addition to the above model tests, it is also necessary to undertaken relevant numerical simulation and numerical model verification [37,38].

Furthermore, to ensure that cast-in-place reinforced concrete underground silos are more sustainable [39–43]—that is, have better waterproof and moisture-proof performance and provide better protection for grain storage, as examined in this study [44–47]—it is necessary to carry out waterproof research on concrete structures [48–50]. Apay et al. [51] investigated the influence of waterproof and water-repellent admixtures on the permeability and compressive strength of concrete. Su et al. [52] presented a review of the composite behavior of the waterproofing membrane interface. Chuai et al. [53] proposed mechanical properties of a prefabricated underground silo steel plate concrete wall. Pisova et al. [54] studied spray-applied waterproofing membranes. However, there is still a lack of research on the composite stress analysis of the bending moment and water pressure of the plastic–concrete wall of underground granaries.

To fill the aforementioned gap, in this study, based on previous references, polypropylene plastic–concrete composite silo wall specimens were designed for an underground granary polypropylene plastic–concrete waterproof system. In addition, the uniformly distributed load test and water pressure load composite test were undertaken on the silo wall specimens, to simulate their stress state in real applications. The deformation, strain evolution, failure mode, and failure mechanism of the specimen under the combined action of the bending moment and water pressure were analyzed. Based on the experimental results, the numerical model was established and the parameters affecting the design of the silo wall were analyzed. This can provide an example for the design of the silo wall of underground granary.

2. Experimental Design

2.1. Test Specimen Design and Manufacture

The test specimen was composed of a polypropylene plastic (PP) waterproof plate, a PP bolt, a PP connecting plate, and a concrete plate. The PP connecting plate and PP waterproof plate were connected by a weld, and the PP bolt and PP connecting plate were connected by the thread and weld. The structure of the test specimen is shown in Figure 1. The dimensions of the square section of PP waterproof plate are 1800 mm × 1800 mm. Five rows and five columns of PP connecting plates were arranged inside the specimen, and the central spacing of the PP connecting plates was 300 mm.

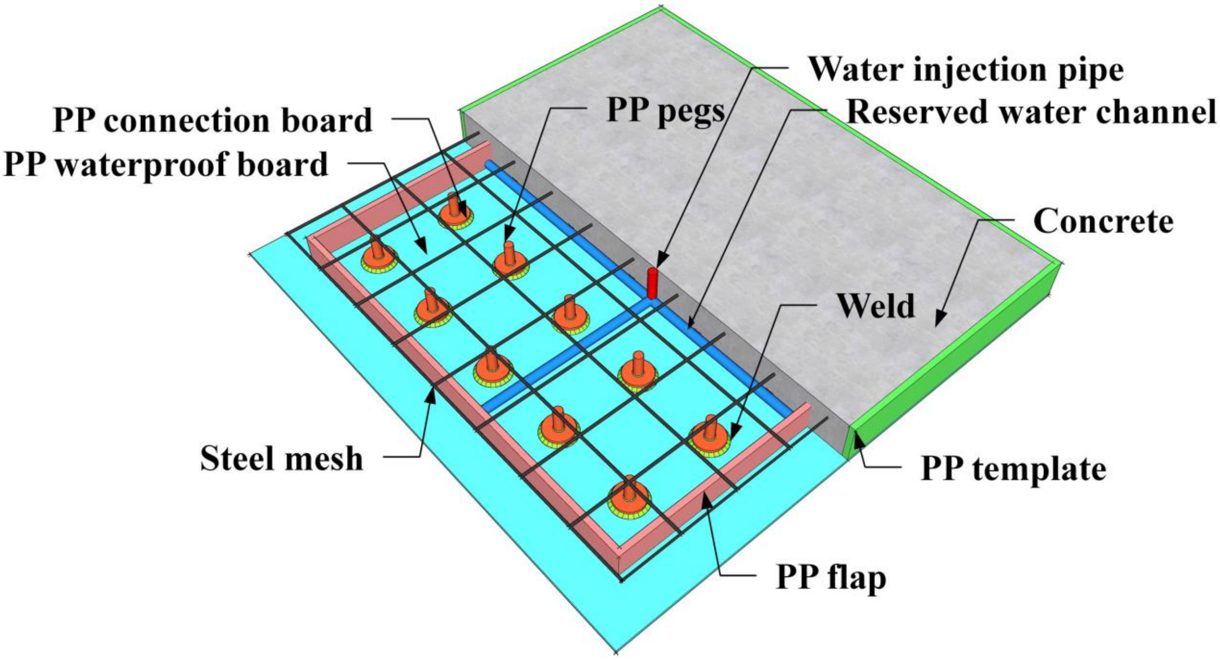

Figure 1. Schematic diagram of test specimen.

In order to take full advantage of the pull-out force of the bolt, the diameter of the PP bolt was 30 mm, its length was 100 mm, and the whole length of the surface of the bolt was covered in turning wire. According to the standard [55,56] of the ordinary thread, the diameter, and the pitch series, in the experiment, the thread height was 0.3 mm and the pitch distance was 1.5 mm. The diameter of the PP connecting plate was 100 mm, and the thickness was 20 mm. In order to enhance the weld strength, the welds of six polypropylene plastic electrodes were utilized to connect the waterproof plate and the connecting plate. The thickness of the waterproof plate, of 10 mm, was selected to be practical and economical. Plastic formwork was arranged around the waterproof plates as pouring formwork.

In addition, a waterproof plastic plate was included. The plastic template, waterproof plastic plate, and the PP waterproof plate were connected by welding. In order to allow water to flow into the specimen, the method of embedding reinforcement was used to reserve a water injection channel in the specimen. After the concrete was set, the embedded reinforcement was extracted, and the plastic plate and plastic template were blocked by planting reinforcement glue. The internal steel mesh of the specimen was arranged using HRB400 double-layer rebar of 8 mm diameter with 200 mm space. Four hooks with a diameter of 16 mm were embedded in the corners of the specimen. The thickness of the concrete protective layer was set to 40 mm, and the concrete strength was C40.

2.2. Test Device

The specimen was placed on a supporting roller having a span of 1500 mm, and the center line of the roller was 150 mm from the edge of the specimen. A movable hinge support and fixed hinge support were each fixed on one side. The test loading was divided into two stages: uniform loading and water pressure loading. In the uniform loading stage, a cast iron weight was used for graded loading; the pressure was increased by 3.79 kN/m^2, which was maintained for 15 min at each stage, and remained unchanged after sequential loading to 21.21 kN/m^2. A hydrostatic water pressure press was used for water pressure loading, which was composed of a pressure pump, pressure control host, and computer control system.

During the water pressure loading, the water pressure was increased by 10 kPa from an initial value of 10 kPa. The pressure was maintained for 3 min at each stage, and the displacement and strain were recorded. The schematic diagram of specimen loading is presented in Figure 2.

Figure 2. Schematic diagram of test loading.

2.3. Test Method

In order to assess the strain distribution of specimens under the combined action of the bending moment and water pressure, 80 strain measuring points, numbered Y1-4 to Y25-3, were arranged at the weld joints inside the PP waterproof plate. Forty strain measuring points were arranged in the middle of the span of the two nodes on the outside of the PP waterproof plate, numbered YL-1 to YL-40. Sixteen strain measuring points were arranged in the middle of the four-node span, numbered YS-1 to YS-16. Ten strain gauges, numbered YC-1 to YC-10, were arranged on the concrete surface, as illustrated in Figure 3.

Furthermore, to measure the maximum displacement and the displacement at the joints of the PP waterproof plate, and to explore the displacement change rule of the specimen, 25 displacement measuring points were arranged at the outer joints of the PP waterproof plate, numbered WJ-1 to WJ-25, and 16 displacement measuring points were arranged at the middle of the four-node span, numbered WS-1 to WS-16, as shown in Figure 4.

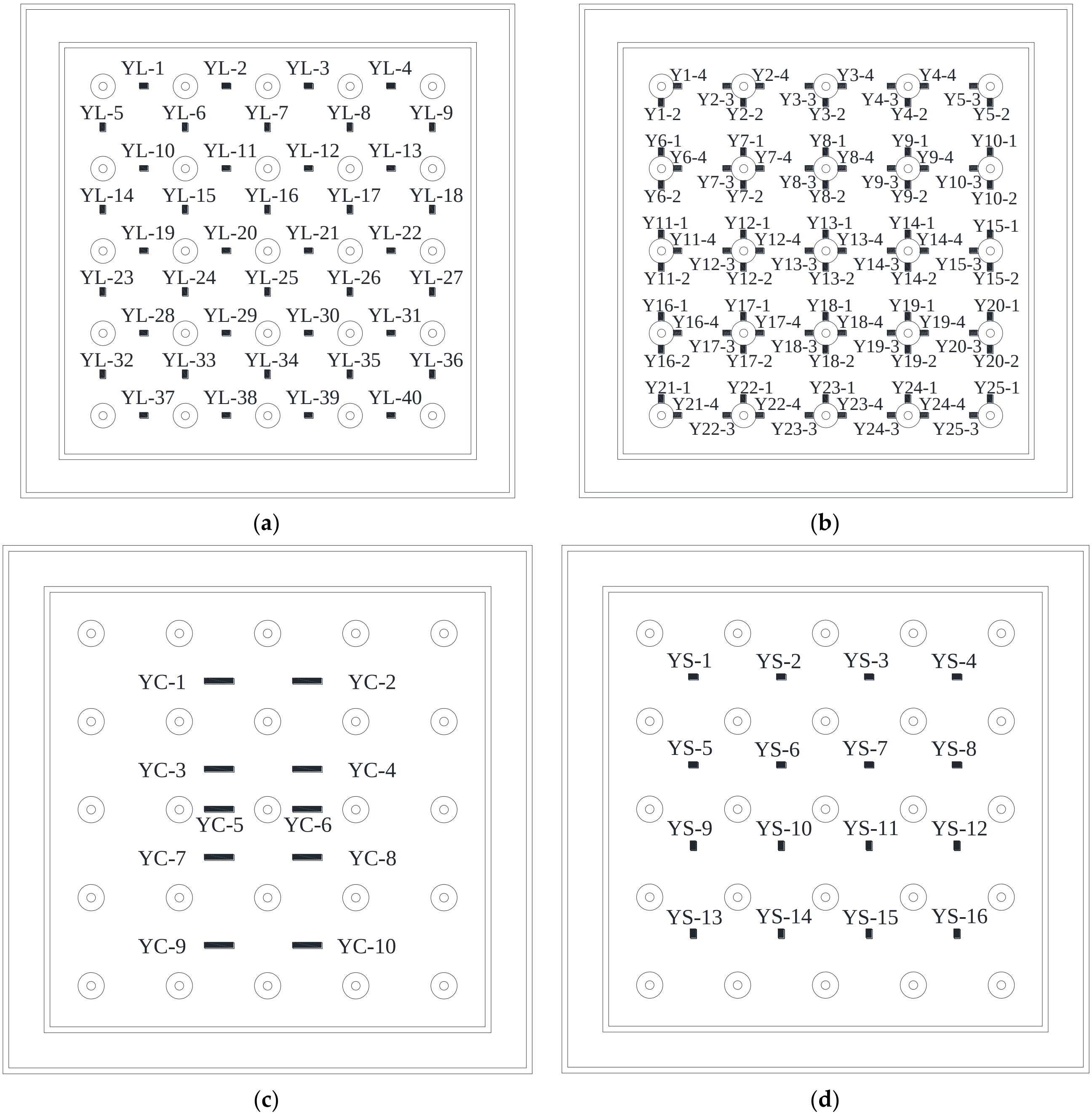

Figure 3. Layout of strain measuring points: (**a**) two-node mid-span strain measuring point; (**b**) strain measuring point at the weld; (**c**) four-node mid-span strain measuring point; (**d**) concrete strain measuring point.

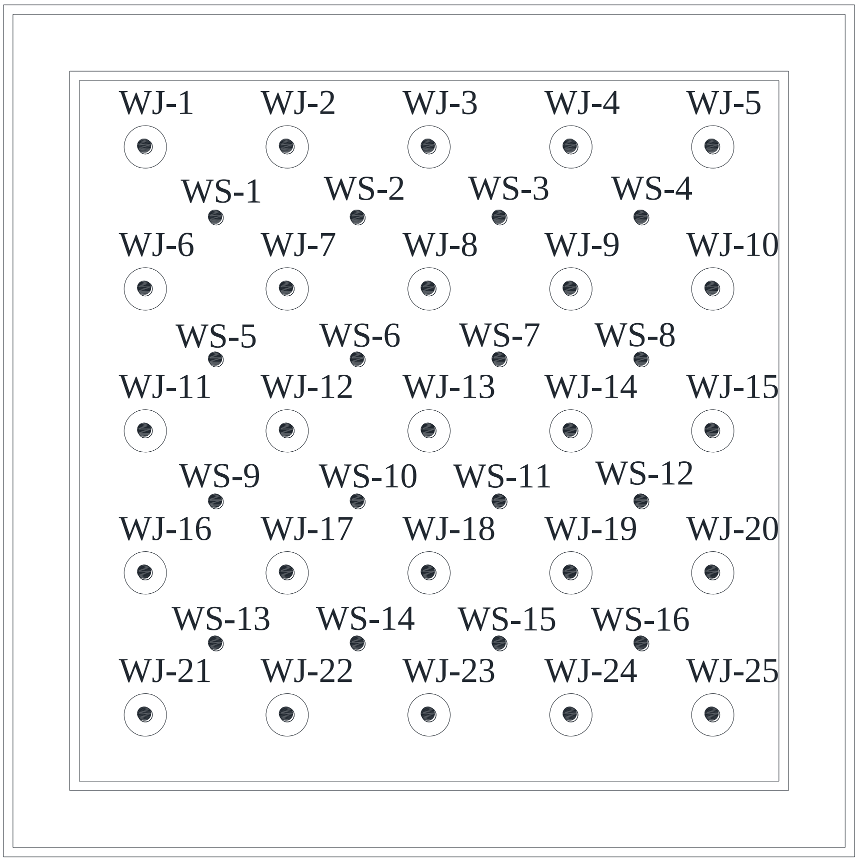

Figure 4. Layout of displacement measuring points.

3. Test Results Analysis

3.1. Failure Mode

The test loading was divided into two stages: uniform load loading and water pressure loading. In the stage of uniform load loading, the deformation of the specimen was small, in general. When the target load was 21.21 kN/m^2, the load pressure was kept unchanged. Then, when the pressure was increased to 76 kPa, the No. WJ-20 node was damaged, and the water pressure in the specimen dropped to 63 kPa at that time. When the water pressure was loaded to 85 kPa, the PP waterproof plate was damaged. The failure position of the specimen is shown in Figure 5a. The waterproof plate at node WJ-19 was cut, as presented in Figure 5b; the weld between the connecting plate and waterproof plate at this node was torn, although the bolts and the connecting plate were well-connected.

The damage to the PP waterproof plate can be explained as follows. At that moment, because of the uneven distribution of water pressure, stripping occurred in the plastic stud slip of the WJ-13 node. The waterproof plate and concrete were first located near the water concentration, and the force of the near node increased, which led to the weld tearing failure of the WJ-19 node. After the destruction of the WJ-19 node, with the increase in water pressure, the weld stress of the nearby nodes increased again, leading to the failure of the WJ-20 node. After the two nodes were damaged, the span of the waterproof plate increased, resulting in the increment in its deformation. Finally, the shear failure of the PP waterproof plate occurred.

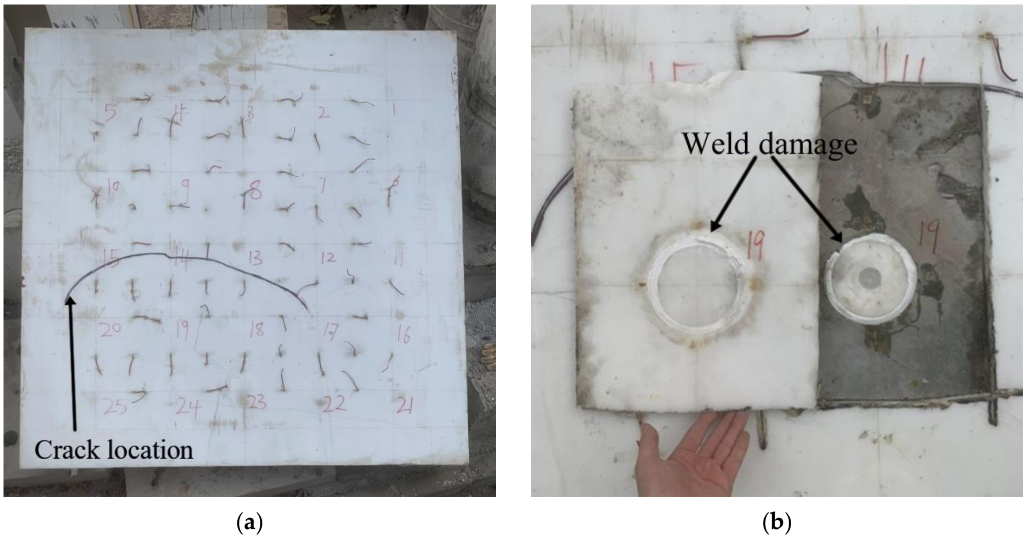

Figure 5. Schematic diagram of specimen damage: (**a**) destruction of the waterproof plate; (**b**) node destruction.

According to the test results, when the PP waterproof plate was damaged, the pressure of the plastic–concrete composite silo wall specimen was 85 kPa. The slip of the plastic bolt in concrete had a great influence on the internal force of the plastic member. The joint weld strength determined the bearing capacity of the plastic waterproof plate. By increasing the joint weld strength, the water pressure-bearing capacity of the silo wall specimen could be improved.

3.2. Load–Displacement Relationship

3.2.1. Load–Displacement Curve of the Node

The displacement at each node increased linearly with the increase in uniform distributed load. When the load reached the maximum value of 21.21 kN/m^2, the maximum displacement of 1.25 mm appeared at No. WJ-23. The displacement–load curve is shown in Figure 6a.

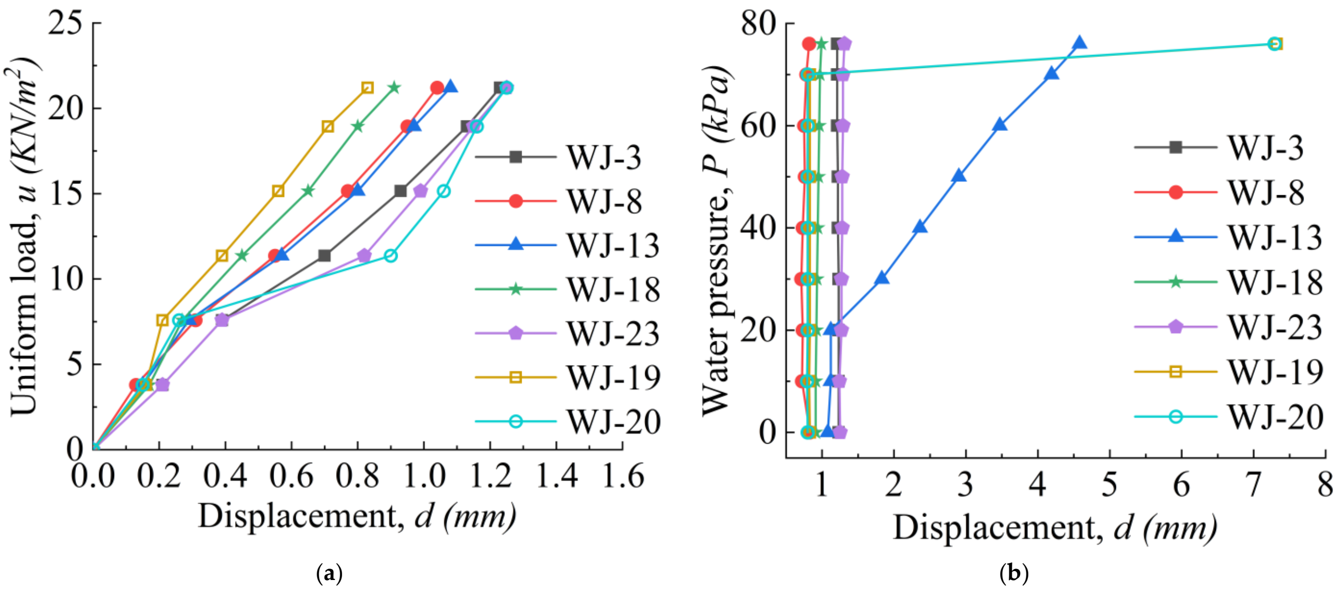

Figure 6. Node displacement–load: (**a**) displacement–uniform load; (**b**) displacement–water pressure.

When the water pressure was less than 20 kPa, the displacement at most nodes did not change significantly with the increase in the water pressure. When the water pressure reached 20 kPa, the displacement of the WJ-13 node increased with the increase in the water pressure, and they showed a linear relationship. The water–displacement curve is shown in Figure 6b.

When the water pressure reached 76 kPa, the maximum displacement of the WJ-13 node was 4.58 mm, and the displacement of WJ-19 and WJ-20 nodes was 7.32 and 7.29 mm, respectively. Comprehensive analysis showed that, in the process of water pressure loading, the plastic stud of the WJ-13 node slipped in the concrete, the waterproof plate near the node and concrete was peeled off, the water flow was concentrated, and the stress on the nearby node increased, leading to the weld tear and failure of the WJ-19 node. The results also showed that the distribution of water pressure was not uniform, in general, and the strength of the joint weld had a significant effect on the water pressure-bearing capacity of specimens.

3.2.2. Four-Node Mid-Span Load–Displacement Relationship

The displacement of the measuring point of the four-node span of the specimen increased with the increase in the uniform distributed load, and showed a linear relationship. When the maximum load reached 21.21 kN/m^2, the maximum displacement appeared at the measuring point of WS-13, with a value of 1.59 mm, as shown in Figure 7a.

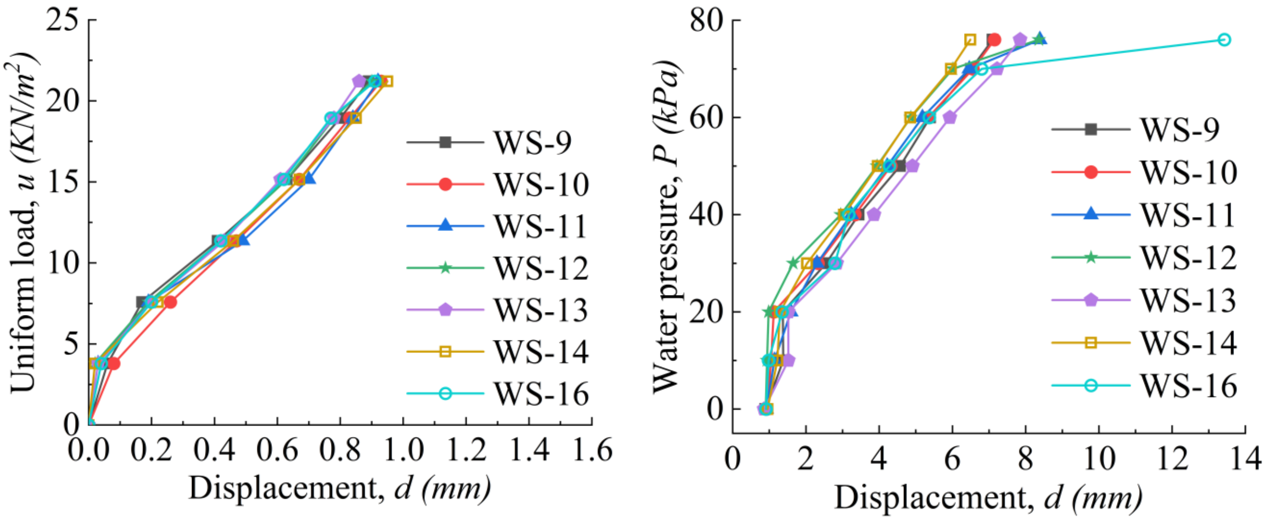

Figure 7. Four-node mid-span displacement–load: (**a**) displacement–uniform load; (**b**) displacement–water pressure.

When the water pressure was less than 20 kPa, its displacement did not change significantly; when the water pressure was greater than 20 kPa, its displacement increased with the increase in the water pressure; when the water pressure reached 76 kPa, the maximum displacement appeared at WS-16 with a maximum value of 12.66 mm, as presented in Figure 7b.

Therefore, during the water pressure loading, because of the chemical adhesive force between the PP waterproof plate and the concrete, when the water pressure was low, displacement of each measuring point resulted in no obvious change. With the increase in water pressure, the PP waterproof plate and concrete were stripped, the measuring point displacement began to change, the water pressure reached the maximum, and the weld of the WJ-19 node was damaged, causing the displacement of the measuring point WS-16. The results showed that the chemical adhesive force between the PP waterproof plate and the concrete could resist part of the water pressure.

3.3. Strain–Load Relationship

3.3.1. Mid-Span Strain–Load Relationship of Two Nodes

Under the uniform distributed load, the mid-span strain of the two nodes increased with the increase in load, and they had a linear relationship. When the load was 21.21 kN/m^2, the maximum strain was 0.000172, which was located at the measurement point YL-21, as shown in Figure 8a. In the process of water pressure loading, when the water pressure was less than 20 kPa, the strain changed slightly. When the water pressure was larger than 20 kPa, the strain linearly increased with the increasing water pressure. As the water pressure reached 76 kPa, the maximum strain of 0.008 occurred at the measurement point YL-15, as presented in Figure 8b.

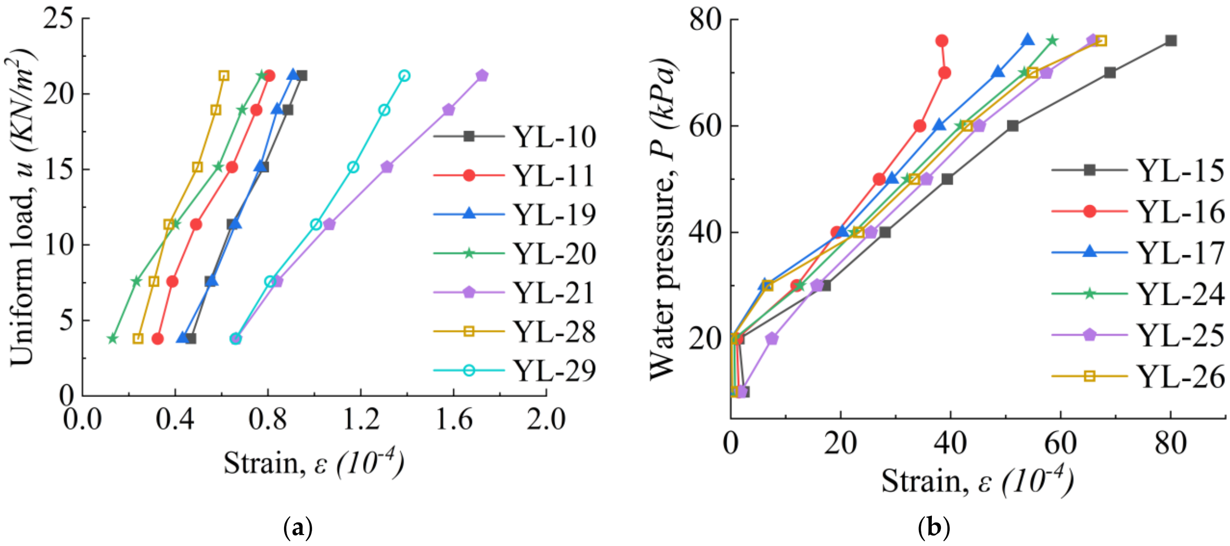

Figure 8. Mid-span strain–load at two nodes: (**a**) strain–uniform load; (**b**) strain–water pressure.

3.3.2. Mid-Span Strain–Load Relationship of Four Nodes

Under the uniform distributed load, the mid-span strain of four nodes increased with the increase in load. When the uniform distributed load was increased to 21.21 kN/m^2, the maximum strain was 0.000146, which was located at the measurement point YS-5, as shown in Figure 9a. When the water pressure was less than 20 kPa, the strain changed little; when the water pressure was larger than 20 kPa, the strain increased with the increase in the water pressure, indicating a linear relationship. When the water pressure was loaded to 76 kPa, the maximum strain was 0.0035, which was located at the measurement point YS-2, as illustrated in Figure 9b.

3.3.3. Nodal Strain–Load Relationship

Under the uniform distributed load, the strain of the waterproof plate at the joint weld increased with the increase in load. When the uniform load was increased to 21.21 kN/m^2, the maximum strain appeared at Y23-4, with a value of 0.000152, as shown in Figure 10a. When the water pressure was larger than 20 kPa, the strain increased with the increase in the water pressure. When the water pressure reached 76 kPa, the strain at the measuring point Y19-3 increased sharply, by 0.002676, as presented in Figure 10b. Comprehensive analysis shows that the joint strain distribution was not uniform and the stress state was complex when the water pressure was loaded. This was because the strain measuring point was located near the weld, and the stress concentration generated at the weld had a great influence on the measuring point.

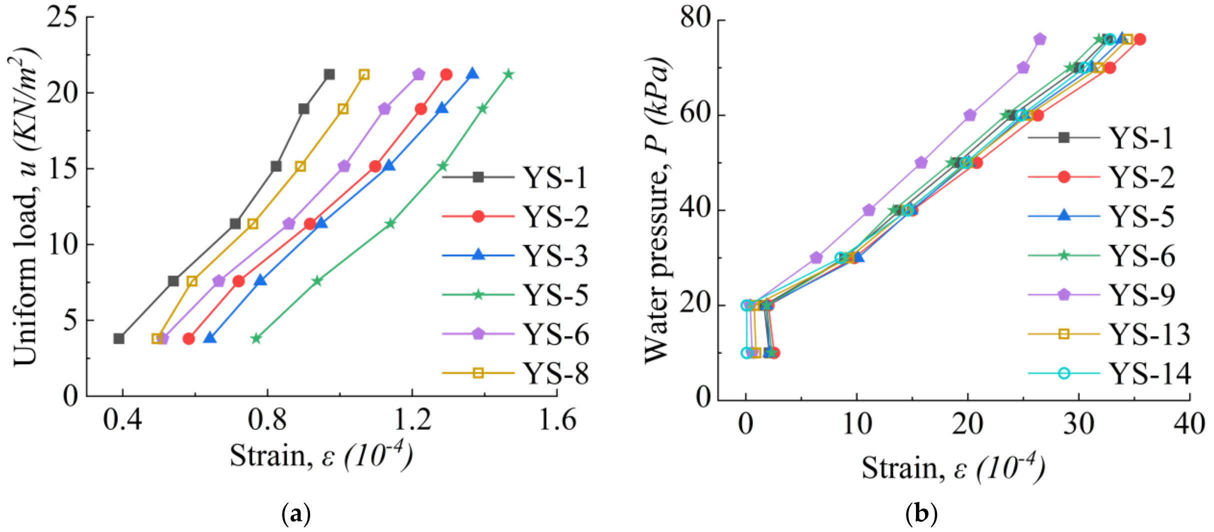

Figure 9. Four-node mid-span strain–load: (**a**) strain–uniform load; (**b**) strain–water pressure.

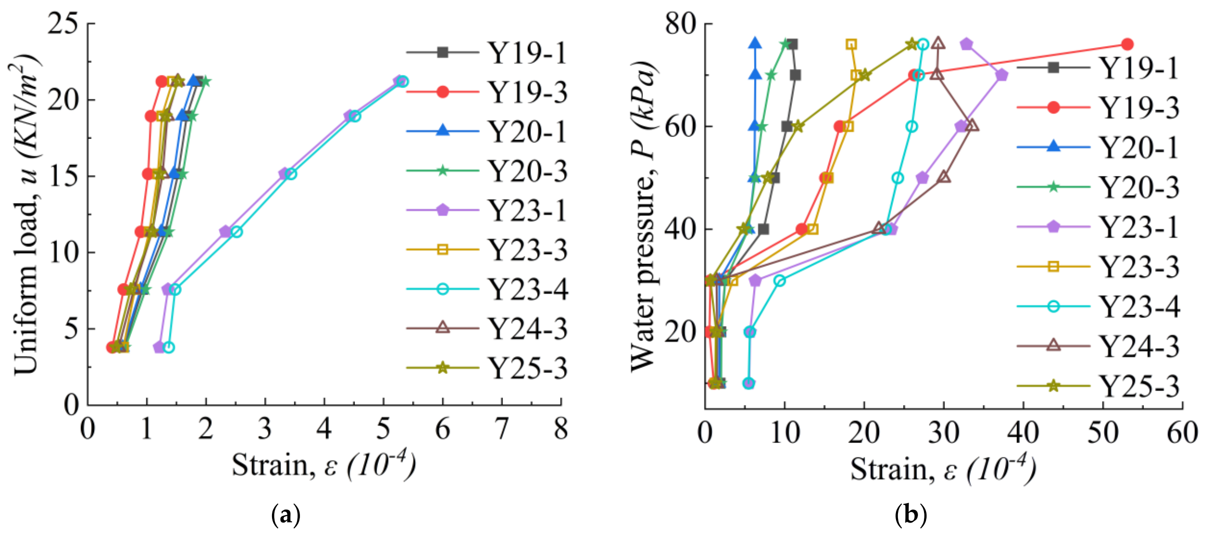

Figure 10. Nodal strain–load relationship: (**a**) strain–uniform load; (**b**) strain–water pressure.

3.3.4. Concrete Surface Strain–Load Relationship

Under the uniform distributed load, the surface strain of concrete increased with the increase in load. When the load was 21.21 kN/m^2, the strain at each measuring point reached the maximum value, which was 0.000124, located at YC-5, as shown in Figure 11a. During the stage of water pressure loading, the concrete surface was always under pressure. However, the strain on the concrete surface changed little, and the influence of water pressure on the concrete was very small and could even be ignored, as indicated in Figure 11b.

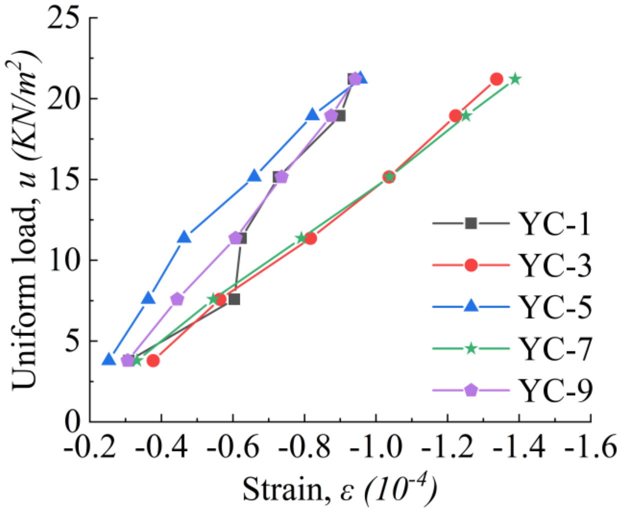

(**a**) (**b**)

Figure 11. Concrete strain–load curve: (**a**) strain–uniform load; (**b**) strain–water pressure.

4. Numerical Modeling

4.1. Constitutive Relation of Materials

In the numerical analysis, the material properties of polypropylene plastics were measured according to [57]. The sample is presented in Figure 12, and the stress–strain curve obtained through the tensile test is shown in Figure 13. The elastic modulus Poisson ratio, tensile yield stress, and tensile yield strain are 1430 MPa, 0.48, 21.5 MPa, and 3.7%, respectively.

Figure 12. Test specimens of PP.

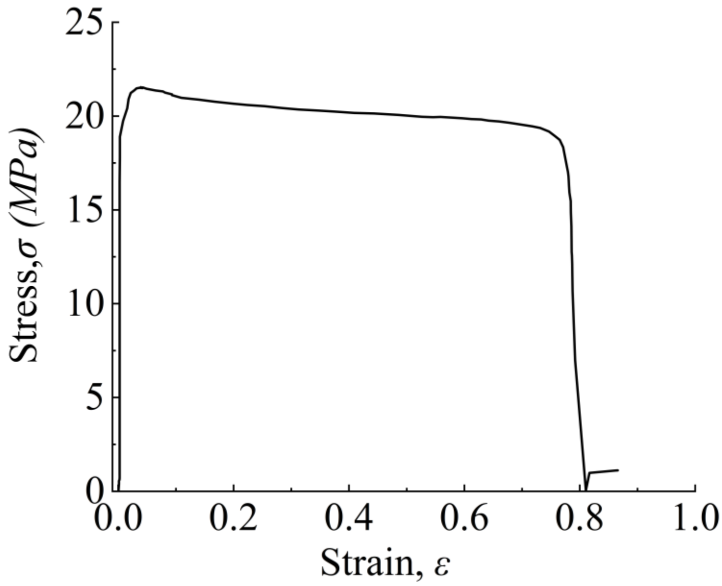

Figure 13. PP stress–strain relationship.

The concrete damaged plastic damage model was implemented in ABAQUS. The relationship between the uni-axial compression and uni-axial tensile stress–strain curve was selected according to [58]. The main parameters of concrete are shown in Table 1. The ideal elastic-plastic model was selected for the steel constitutive model, for which the elastic modulus is 2.1×10^6 MPa and Poisson's ratio is 0.3.

Table 1. Concrete material parameters.

Characteristic	Parameter
Expansion angle α	36.31°
Eccentricity c	0.1
Fb0/fc0	1.16
Shape factor K	0.667
Viscosity parameter μ	0.0005
Poisson's ratio ϑ	0.2

4.2. Cell Selection and Meshing

In order to ensure the accuracy of the numerical results, an eight-node linear hexahedron linear reduction integral element (C3D8R) was used for the PP waterproof plate, PP connecting plate, PP bolt, plastic formwork, watertight plastic plate, and concrete; and the truss element (T3D2) was used for the steel mesh. The grid size of the PP waterproof plate and plastic template was 40 mm, and the grid size of the waterproof plastic plate was 20 mm, as shown in Figure 14a. The grid size of the PP stud and PP connecting plate was 14 mm, as presented in Figure 14b. As the stress of concrete and steel mesh was not the focus of this analysis, the grid sizes of concrete and steel mesh were 60 and 40 mm, respectively. The concrete mesh division is illustrated in Figure 14c.

4.3. Load Application and Boundary Conditions

In the numerical model, the loading form of the force was adopted, and the concrete surface was uniformly loaded and graded to provide the uniform load. Since the water pressure action cannot be accurately predicted in the test, the inner waterproof plate was graded by loading with the most unfavorable uniform load to provide water pressure action. According to the supporting mode of the specimen in the test, X- and Z- directional displacement constraints, rotation constraints, and Y-directional displacement constraints were applied at 150 mm from the bottom of the specimen to the left edge, and X- and

Z-directional rotational constraints and Y- and Z-directional displacement constraints were applied at 150 mm from the bottom of the specimen to the right edge.

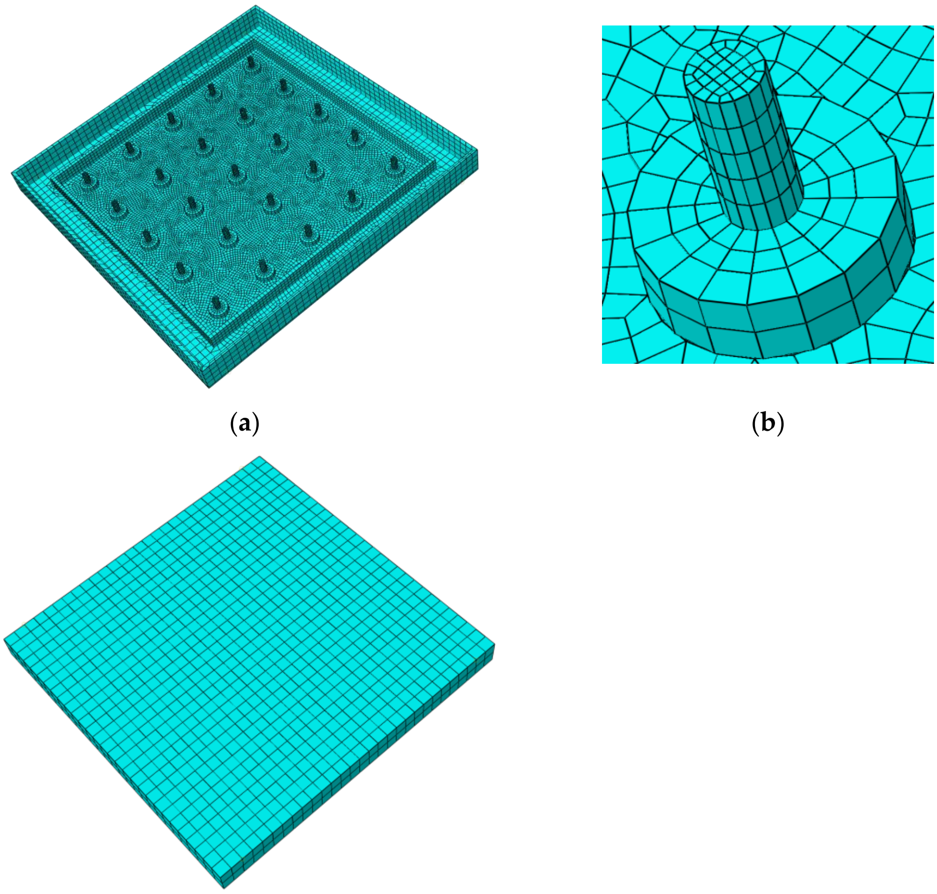

(**a**) (**b**)

(**c**)

Figure 14. Meshing: (**a**) mesh division of PP waterproof plate; (**b**) meshing of pegs and connecting plates; (**c**) concrete meshing.

4.4. Contact Simulation

In ABAQUS, the contact unit was used to simulate the contact interface between the concrete and plastic formwork, and the normal direction of the contact surface was the hard contact. PP pegs and steel mesh were embedded into the concrete through the embedment, and the PP connecting plate was connected to the plastic waterproof plate through the tie.

5. Numerical Model Validation

5.1. Comparison of Load–Displacement Curves

In the uniformly distributed loading stage, the mean values of the mid-span node displacement test and corresponding simulated values of the specimens increased with the increase in load. Furthermore, their variation trends were consistent and their relative differences ranged from −8.71% to 4.78%, indicating that the numerical analysis results were in good agreement with the test results, as can be seen in Figure 15a.

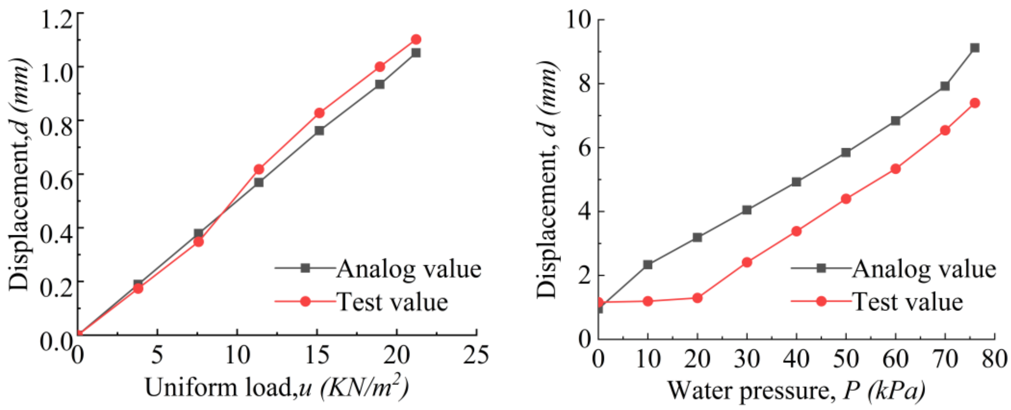

(**a**) (**b**)

Figure 15. Displacement comparison: (**a**) comparison of uniform loading stage; (**b**) comparison of water pressure loading stages.

In the water pressure loading stage, due to the water pressure distribution in the test, the displacement of the four nodes was selected for comparison and analysis; these displacements grew significantly, as shown in Figure 15b.

During the water pressure loading process, the simulation value was greater than the value in the experiment. When the water pressure was greater than 20 kPa, both values showed the same trend, having a relative difference between −18% and 145%. The main reasons for this are as follows: in the numerical analysis, the water pressure was loaded according to the most unfavorable loading of the water pressure; it was also assumed that the waterproof plate is under uniform pressure, and size values for loading were the same as those for the water pressure test. However, in the actual test, the direction of flow of the injection between the waterproof plate and the concrete was randomly distributed, and the size of the water area on the waterproof plate also varied randomly and was unpredictable. Therefore, during the water pressure loading stage, the size and mode of numerical loading were inconsistent with those of the test loading, leading to a large relative difference between the numerical simulation value and the test value, although the overall trends were consistent.

5.2. Comparison of Load–Strain Curves

Under the combined action of the bending moment and water pressure, the tensile stress of the waterproof plate near the weld joint of the specimen was large. The strain of the measuring point Y9-1 at the weld joint was selected for comparative analysis.

Under the uniformly distributed load, the test values and the corresponding simulation values increased with the load, and both showed a linear growth trend, whose relative difference was between −0.1% and 17%. Generally, they are in good agreement, as shown in Figure 16a. The relative difference is mainly due to the fact that the test point was close to the plastic weld seam of the strain, which had a greater influence on the measuring point of stress concentration.

In the water pressure loading stages, the early stage of the load simulation had a value greater than the test values. With the increase in water pressure, the test value gradually became greater than the simulation value. The values showed the same variation trend, and the relative difference was between −47.7% and 17%, as shown in Figure 16b. This difference was mainly because of the stress concentration caused by the node welds, and the difference in the water pressure loading method between the numerical simulation and the experiment.

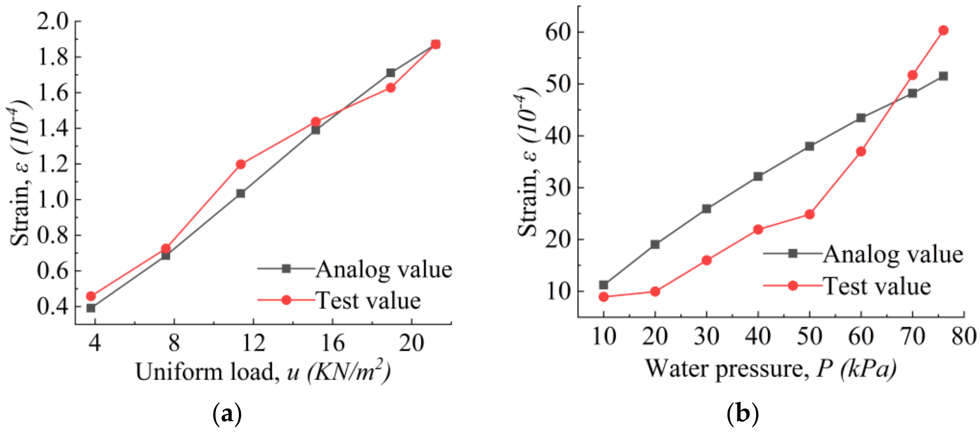

Figure 16. Strain comparison: (**a**) comparison of uniform loading stage; (**b**) comparison of water pressure loading stages.

Through the above comparative analysis, it can be seen that numerical parameters selected in this paper, such as constitutive relation, contact relation, and boundary condition, can better simulate the loading process of the specimen of the silo wall. The modeling method adopted in numerical is effective, and lays a foundation for the parameter analysis in next section.

6. Design Parameter Analysis

Based on the verified parameters of the numerical model, 14 numerical models were established to analyze the design parameters of plastic–concrete composite bin wall specimens, including the spacing and radius of the connecting plate and the thickness of the waterproof plate.

As the direction of water flow cannot be predicted in the test, in the following models, the loaded water pressure was applied uniformly under the most unfavorable condition. The selection of the numerical design parameters and the main results are listed in Table 2. In each model, a parameter was changed according to the basic model, while the other parameters were left unchanged.

The influence of the connection plate spacing, radius, and waterproof plate thicknesses on the internal force were investigated under the combined bending moment and water pressure. The four-node mid-span displacement at WS-7 and the Mises stress at WJ-13 were selected for comparison.

6.1. Connecting Plate Spacing

Under the compound action of the bending moment and water pressure, the mid-span displacement of each specimen at the four joints increased with the increase in the water pressure at different connecting plate spacings. When the stress of the waterproof plate at the joints reached the yield stress of 21.5 MPa, for different connecting plate spacings of 200, 250, 300, 350, and 400 mm, the maximum displacements were 13.04, 19.18, 22.09, 25.94, and 28.68 mm, respectively. The maximum mid-span displacement of four nodes increased with the increase in the spacing between the connecting plates. When the spacing was increased from 200 to 400 mm, the displacement increased by 119.9%, as presented in Figure 17a.

The stress of the waterproof plate at the mid-span joint of each specimen increased with the increase in the water pressure, and the two others both increased linearly. When the stress value reached the PP yield stress of 21.5 MPa, the water pressure of each specimen reached its bearing capacity, as shown in Figure 17b.

Table 2. Design parameters and main results.

Numerical Model Number	PP Connection Plate Spacing (mm)	PP Waterproof Plate Thickness (mm)	PP Connecting Plate Radius (mm)	Water Pressure-Bearing Capacity (kPa)	Peak Displacement (mm)
PCW-R40	300	10	40	230	22.18
PCW-R50			50	300	22.09
PCW-R60			60	380	22.01
PCW-R70			70	400	20.84
PCW-R80			80	420	19.12
PCW-B8	300	8	50	240	24.63
PCW-B10		10		300	24.28
PCW-B12		12		350	22.28
PCW-B14		14		380	21.91
PCW-B16		16		350	21.71
PCW-B18		18		360	20.88
PCW-D200	200	10	50	650	13.04
PCW-D250	250			450	19.18
PCW-D300	300			300	22.09
PCW-D350	350			200	25.94
PCW-D400	400			150	28.68

Note: PCW is the abbreviation of plastic–concrete wall; R in R40 means connecting plate radius, 40 means radius of 40 mm; B8 means waterproof plate thickness, 8 means thickness of 8 mm; D200 means D means connecting plate spacing, 200 means spacing of 200 mm.

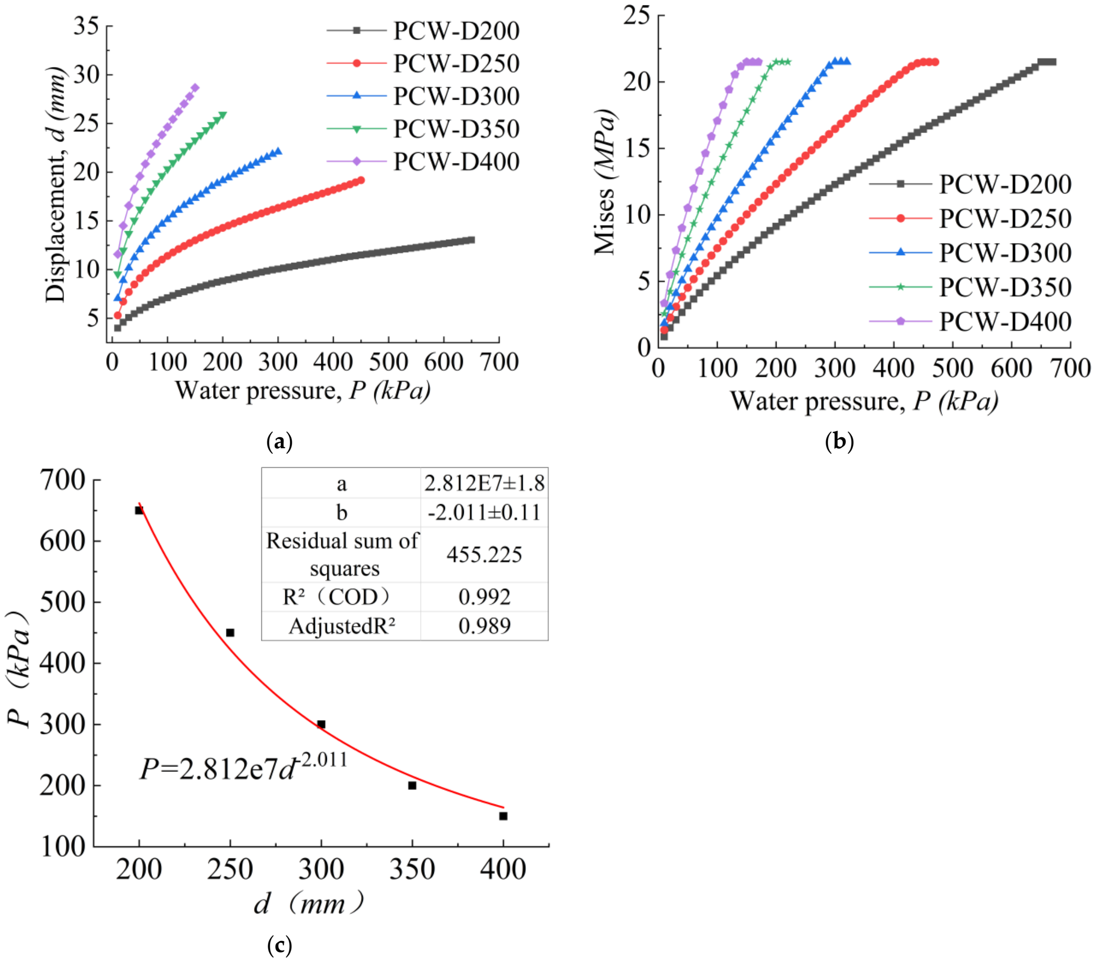

Figure 17. Different connecting plate spacing: (**a**) displacement comparison; (**b**) stress comparison; (**c**) *d*-*P* diagram.

Corresponding to different connecting plate spacings of 200, 250, 300, 350, and 400 mm, the water pressure-bearing capacity of each specimen was 650, 450, 300, 200, and 150 kPa, respectively. When the spacing increased from 200 to 400 mm, the water pressure-bearing capacity decreased by 76.9%. The relationship between the connecting plate spacing and water pressure-bearing capacity is shown in Figure 17c.

It can be seen from Figure 17 that the water pressure-bearing capacity P and connecting plate spacing d have a nonlinear relationship, and their functional relationship can be obtained by fitting as follows:

$$P = 2.812\text{e}7d^{-2.011} \tag{1}$$

where P is the water pressure-bearing capacity, and d is the spacing between PP connecting plate.

The results show that when the radius of the connecting plate and the thickness of the waterproof plate are constant, the distance between the connecting plate has a significant influence on the water pressure-bearing capacity and the corresponding maximum displacement of the specimen. In practical engineering design, by reducing the distance between the connecting plates, the water pressure-bearing capacity and stiffness of the specimen can be effectively improved.

6.2. Connecting Plate Radius

Under the combined action of the bending moment and water pressure, the mid-span displacement of four joints of each specimen increased with the increase in water pressure under different connecting plate radii. For different connecting plate radii of 40, 50, 60, 70, and 80 mm, the maximum displacements were 21.18, 22.09, 22.01, 20.84, and 19.12 mm, respectively.

When the mid-span displacement of the four joints reached the maximum value, and the connection radius was less than or equal to 60 mm, the waterproof plate stress at the mid-span joints reached the PP yield stress. When the connection radius was greater than 60 mm, the PP stud yielded before the waterproof plate. The maximum mid-span displacement of the four nodes decreased as the radius of the connecting plate increased. When the radius increased from 40 to 80 mm, the displacement decreased by 9.7%, as illustrated in Figure 18a.

The stress of the waterproof plate at the mid-span joint of each specimen increased linearly with the increase in water pressure. For different connecting plate radii of 40, 50, 60, 70, and 80 mm, the water pressure-bearing capacity of each specimen was 230, 300, 380, 400, and 420 kPa, respectively. When the radius increased from 40 to 80 mm, the water pressure-bearing capacity increased by 65.2%. When the radius of the connecting plate was less than or equal to 60 mm, and the water pressure of the specimen reached its water pressure-bearing capacity, the stress at the joints of the waterproof plate reached the PP yield stress. When the radius of the connecting plate was greater than 60 mm, and the water pressure of the specimen reached its water pressure-bearing capacity, the stress at the joints of the waterproof plate did not reach its yield stress. At this time, the PP bolt in the specimen reached the yield before the waterproof plate, leading to the failure of the specimen. The relation between the radius of the connecting plate and the water pressure-bearing capacity is shown in Figure 18c.

It can be seen from Figure 18 that the water pressure-bearing capacity P has a nonlinear relationship with the radius of the connecting plate r, and the function relation between them can be obtained by fitting as follows:

$$P = -330.571 + 18.514r - 0.114r^2 \tag{2}$$

where r is the radius of the PP connecting plate.

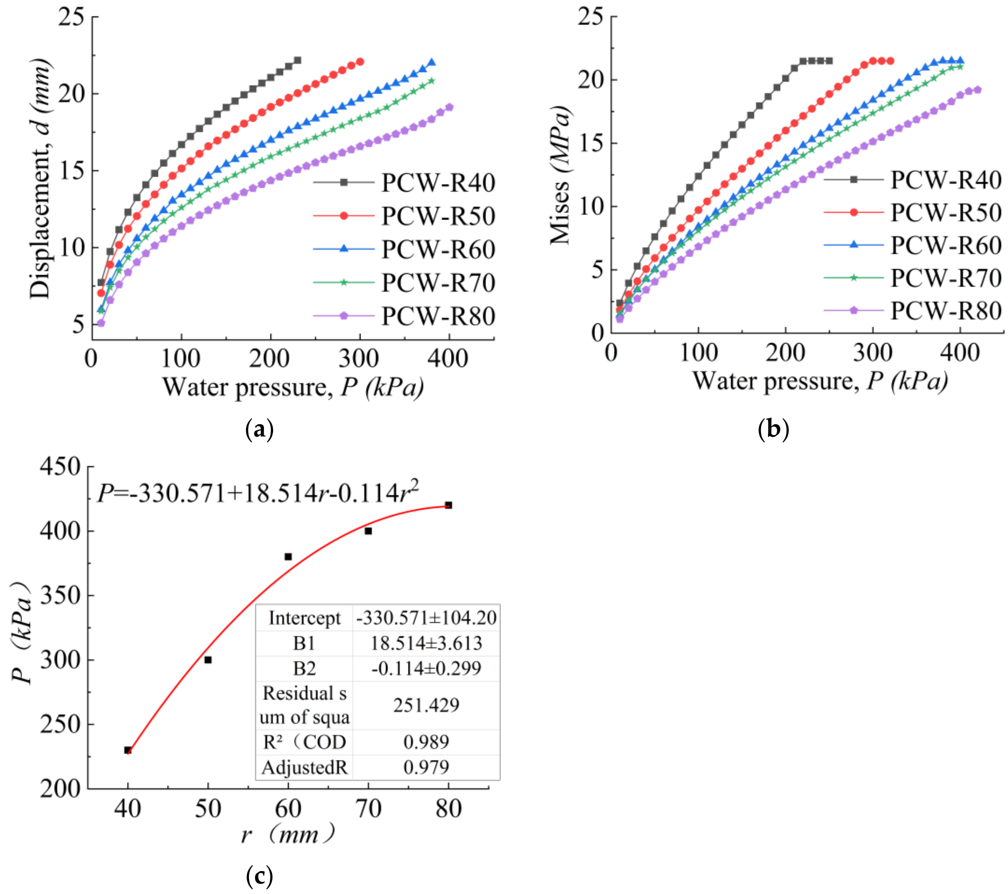

Figure 18. Different connecting plate radii: (**a**) displacement comparison; (**b**) stress comparison; (**c**) *r-P* diagram.

The results show that when the connection plate spacing and waterproof plate thickness are constant, the connecting plate radius of specimen has a greater influence on the hydrostatic-bearing capacity and the corresponding maximum displacement. When the connecting plate radius is greater than 60 mm, the stud strength of specimen becomes the main control factor of damage. When increasing the radius of the connection plate in the engineering design, to improve the hydrostatic-bearing capacity of the specimens, it is necessary to enhance the strength of the stud at the same time.

6.3. Thickness of Waterproof Plate

Under the compound action of the bending moment and water pressure, the mid-span displacement of four joints of each specimen increased with the increase in water pressure under different thicknesses of the waterproof plate, i.e., 8, 10, 12, 14, 16, and 18 mm. The maximum displacements were 24.63, 24.24, 22.28, 21.91, 21.71, and 20.88 mm, respectively. When the mid-span displacement of the four joints reached the maximum value and the thickness of the waterproof plate was less than or equal to 14 mm, the stress at the joints of the waterproof plate reached the PP yield stress. When the thickness of the waterproof plate was greater than 14 mm, the PP bolt yielded before the waterproof plate. The maximum mid-span displacement of the four nodes decreased with the increase in the plate thickness. When the plate thickness increased from 8 to 18 mm, the displacement decreased by 11%, as shown in Figure 19a.

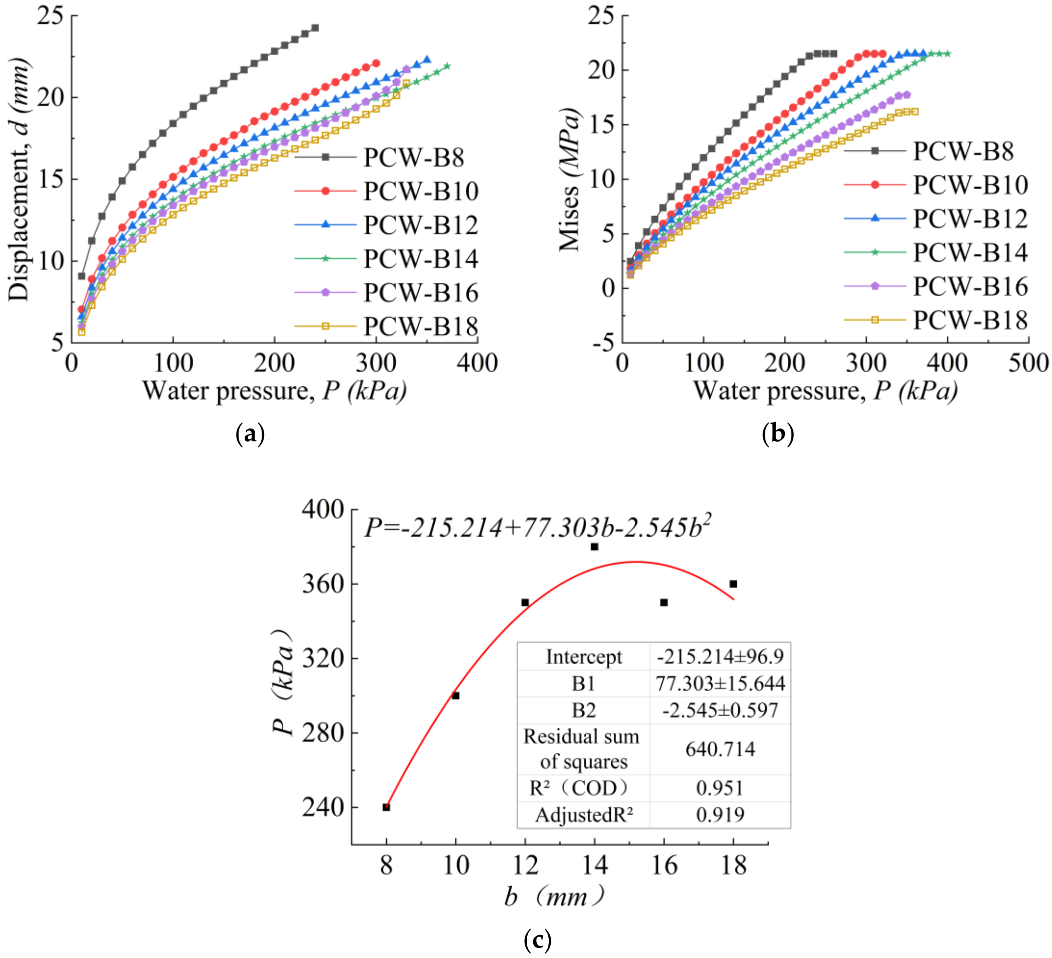

Figure 19. Different thicknesses of waterproof plate: (**a**) displacement comparison; (**b**) stress comparison; (**c**) *b*-*P* diagram.

The stress of the waterproof plate at the mid-span joint of the specimen increased with the increase in water pressure, and they both increased linearly. For different plate thicknesses of 8, 10, 12, and 14 mm, when the stress at the joints of waterproof plates reached the yield stress, the water pressure-bearing capacity of specimens reached 240, 300, 350, and 380 kPa, respectively. For different plate thicknesses of 16 and 18 mm, the stud reached the yield stress earlier than the waterproof plate, and the water pressure-bearing capacity of the specimens was 350 and 360 kPa, respectively. The relation between the thickness of the waterproof plate and the water pressure-bearing capacity is given in Figure 19c.

It can be seen from Figure 19 that the relation between the water pressure-bearing capacity P and the thickness of the waterproof plate b is nonlinear, and the function relation between them can be obtained by fitting as follows:

$$P = -215.214 + 77.303b - 2.545b^2 \quad (3)$$

where b is the thickness of the PP waterproof plate.

The results show that the thickness of the waterproof plate has a great influence on the water pressure-bearing capacity and the corresponding maximum displacement, when the radius and spacing of the connecting plate are constant. When the thickness of waterproof plate is greater than 14 mm, the specimen failure depends on the bolt strength. Therefore, the water pressure-bearing capacity can be improved by increasing the bolt strength in practical engineering.

6.4. Parameter Sensitivity Analysis

Taking the water pressure-bearing capacity of the plastic–concrete composite silo wall specimens as the dependent variable, multiple linear regression analysis was conducted with the spacing d of the connecting plates, radius R of the connecting plates, and thickness B of the waterproof plates as independent variables. The obtained regression parameters are summarized in Table 3.

Table 3. Regression parameters.

Project	Coefficient	Standard Error	Regression Coefficients (Beat)	T-Statistic	Significance
Constant	788.303	120.865	-	6.552	0.000
d	−2.500	0.279	−0.874	−8.969	0.000 *
r	4.074	1.216	0.330	3.350	0.006 *
b	7.775	4.377	0.175	1.776	0.101 **

Note: At the significance level of 0.05, * means significant, ** means not significant.

As can be seen from Table 3, the best values of connection plate spacing, connection plate radius, and waterproof plate thickness were −0.874, 0.330, and 0.175, respectively, indicating that the connection plate spacing has the greatest (and negative) correlation with the water pressure-bearing capacity of the specimen, followed by the connection plate radius, which has a positive correlation; the waterproof plate thickness has a small influence on the water pressure-bearing capacity of the specimen. It can be seen from the significance that the connecting plate spacing and its radius are significant, whereas the thickness of the waterproof plate is not. Based on the load design value, the distance between the connecting plates should be reduced, or the radius of the connecting plates should be increased to improve the water pressure-bearing capacity of the specimens.

7. Conclusions

In this study, the internal force, deformation, failure mechanism, and water pressure-bearing capacity of the plastic–concrete composite silo wall under the combined action of the bending moment and water pressure were examined by means of uniform loading and water pressure loading tests and numerical analysis. The following conclusions can be drawn:

(1) During the uniform loading stage, the plastic plate and concrete in the plastic–concrete composite specimen worked together through the plastic bolt, and the displacement and strain of the waterproof plate increased linearly with the increase in the load; however, their values were changed little. During the stage of water pressure loading, under the compound action of the bending moment and water pressure, the displacement and strain of the waterproof plate increased significantly with the increase in water pressure.

(2) There was a chemical adhesive force between the PP waterproof plate and concrete, which could resist the 20 kPa water pressure. Under a certain uniform load, with the increase in water pressure, the waterproof plate and concrete in the specimen gradually peeled off, and their combined effect was gradually weakened. Regarding the PP waterproof plate shear failure, the maximum water pressure was 85 kPa.

(3) The numerical model of the plastic–concrete composite silo wall was established. The numerical analysis results were in good agreement with the test results, which shows that the numerical model is accurate and feasible. Based on the numerical analysis results, the expressions of the relationship between the design parameters and the water pressure-bearing capacity were presented.

(4) When the thickness of the waterproof plate is larger than 14 mm or the radius of the connecting plate is larger than 60 mm, the bolt strength is the main control factor of specimen failure. When increasing the thickness of the waterproof plate or the

radius of the connecting plate to improve the water pressure-bearing capacity of the specimen, the bolt strength should also be enhanced.

(5) The numerical parameter analysis shows that, compared with the thickness of the waterproof plate, the connection plate spacing and its radius have a greater influence on the water pressure-bearing capacity of the specimen. The regression coefficients of the connection plate spacing, radius, and waterproof plate thickness on the water pressure-bearing capacity of the specimen were −0.874, 0.330, and 0.175, respectively.

Author Contributions: Conceptualization, H.Z. and J.Y.; methodology, H.Z.; software, K.H.; validation and formal analysis, J.Y.; data curation, L.C.; writing—original draft preparation, K.H.; writing—review and editing, H.Z. All authors have read and agreed to the published version of the manuscript.

Funding: This research was funded by the National Natural Science Foundations of China (Grant No. 52108134), the Fund Project of scientific and technological breakthrough of Henan province (Grant No. 202102110122, 212102110200), and the School Research Fund for the Doctoral Program (Grant No. 31401223).

Informed Consent Statement: Informed consent was obtained from all subjects involved in the study. Written informed consent has been obtained from the patient.

Data Availability Statement: The data used to support the findings of this study are available from the corresponding author upon request.

Acknowledgments: This work is supported by National Ministry of Science and Technology 2014 Special Project for Food Public Welfare Industry "Research and Development of the New Ware-house Type and Technical Systems for Ecological Grain Storage" (Grant No. 201413007).

Conflicts of Interest: The author declares no potential conflicts of interest regarding the publication of this article.

Author Recommendation: In future research, a more comprehensive analysis will be focused on the effect of different connection plate radii, spacings, and waterproof plate thicknesses on the stress of the plastic–concrete silo wall. In addition, water pressure distribution regularity between the waterproof plate and concrete will be investigated.

References

1. Pan, Y.; Fang, H.; Li, B.; Wang, F. Stability analysis and full-scale test of a new recyclable supporting structure for underground ecological granaries. *Eng. Struct.* **2019**, *192*, 205–219. [CrossRef]
2. Valls, A.; García, F.; Ramírez, M.; Benlloch, J. Understanding subterranean grain storage heritage in the Mediterranean region: The Valencian silos (Spain). *Tunn. Undergr. Space Technol.* **2015**, *50*, 178–188. [CrossRef]
3. Zhang, X.; Zhang, H.; Wang, Z.; Chen, X.; Chen, Y. Research on the temperature field of grain piles in underground grain silos lined with plastic. *J. Food Process Eng.* **2022**, *45*, e13971. [CrossRef]
4. Sirousazar, M.; Yari, M.; Achachlouei, B.F.; Arsalani, J.; Mansoori, Y. Polypropylene/montmorillonite Nanocomposites for Food Packaging. *e-Polymersb* **2016**, *7*, 305–313. [CrossRef]
5. Gong, C.; Ding, W.; Mosalam, K.M. Performance-based design of joint waterproofing of segmental tunnel linings using hybrid computational/experimental procedures. *Tunn. Undergr. Space Technol.* **2020**, *96*, 103172. [CrossRef]
6. Gong, C.; Ding, W.; Soga, K.; Mosalam, K.M. Failure mechanism of joint waterproofing in precast segmental tunnel linings. *Tunn. Undergr. Space Technol.* **2018**, *84*, 334–352. [CrossRef]
7. Xu, Q.; Zhang, H.; Liu, Q.; Wang, L. Seismic analysis on reinforced concrete group silos through shaking table tests. *Struct. Concr.* **2020**, *22*, 1285–1296. [CrossRef]
8. Ho, N.; Doh, J. Prediction of ultimate strength of concrete walls restrained on three sides. *Struct. Concr.* **2019**, *20*, 942–954. [CrossRef]
9. Farajzadehha, S.; Mahdikhani, M.; Moayed, R.Z.; Farajzadehha, S. Experimental study of permeability and elastic modulus of plastic concrete containing nano silica. *Struct. Concr.* **2020**, *23*, 521–532. [CrossRef]
10. Khatib, J.; Jahami, A.; Elkordi, A.; Abdelgader, H.; Sonebi, M. Structural Assessment of Reinforced Concrete Beams Incorporating Waste Plastic Straws. *Environments* **2020**, *7*, 96. [CrossRef]
11. Massone, L.M.; Rojas, F.R.; Ahumada, M.G. Analytical study of the response of reinforced concrete walls with discontinuities of flag wall type. *Struct. Concr.* **2017**, *18*, 962–973. [CrossRef]
12. Babaei, A.; Mortezaei, A.; Salehian, H. Experimental study on seismic performance of steel fiber reinforced concrete wall piers. *Struct. Concr.* **2020**, *22*, 1363–1377. [CrossRef]

13. Scamardo, M.; Cattaneo, S.; Biolzi, L.; Vafa, N. Parametric Analyses of the Response of Masonry Walls with Reinforced Plaster. *Appl. Sci.* **2022**, *12*, 5090. [CrossRef]
14. Lee, C.-B.; Lee, J.-H. Nonlinear Dynamic Response of a Concrete Rectangular Liquid Storage Tank on Rigid Soil Subjected to Three-Directional Ground Motion. *Appl. Sci.* **2021**, *11*, 4688. [CrossRef]
15. Qingzhang, Z.; Zhilong, H.; Hao, Z.; Zhenqing, W.; Da, X. Experimental study on resisted water pressure for connecting welds of polypropylene plastic plates in underground silos. *Plast. Rubber Compos.* **2021**, *1*, 1–9. [CrossRef]
16. Shi, W.; Wang, L.; Lu, Z.; Zhang, Q. Application of an Artificial Fish Swarm Algorithm in an Optimum Tuned Mass Damper Design for a Pedestrian Bridge. *Appl. Sci.* **2018**, *8*, 175. [CrossRef]
17. Jeon, S.-H.; Park, J.-H. Seismic Fragility of Ordinary Reinforced Concrete Shear Walls with Coupling Beams Designed Using a Performance-Based Procedure. *Appl. Sci.* **2020**, *10*, 4075. [CrossRef]
18. Mohamad, A.-B.A.E.; Chen, Z. Experimental Studies on the Behavior of a Newly-Developed Type of Self-Insulating Concrete Masonry Shear Wall under in-Plane Cyclic Loading. *Appl. Sci.* **2017**, *7*, 463. [CrossRef]
19. Hao, T.; Cao, W.; Qiao, Q.; Liu, Y.; Zheng, W. Structural Performance of Composite Shear Walls under Compression. *Appl. Sci.* **2017**, *7*, 162. [CrossRef]
20. Poonyakan, A.; Rachakornkij, M.; Wecharatana, M.; Smittakorn, W. Potential Use of Plastic Wastes for Low Thermal Conductivity Concrete. *Materials* **2018**, *11*, 1938. [CrossRef]
21. Kromoser, B.; Gericke, O.; Hammerl, M.; Sobek, W. Second-Generation Implants for Load Introduction into Thin-Walled CFRP-Reinforced UHPC Beams: Implant Optimisation and Investigations of Production Technologies. *Materials* **2019**, *12*, 3973. [CrossRef]
22. Flores-Johnson, E.A.; Company-Rodríguez, B.A.; Koh-Dzul, J.F.; Carrillo, J.G. Shaking Table Test of U-Shaped Walls Made of Fiber-Reinforced Foamed Concrete. *Materials* **2020**, *13*, 2534. [CrossRef]
23. Al-Fakih, A.; Al-Osta, M.A. Finite Element Analysis of Rubberized Concrete Interlocking Masonry under Vertical Loading. *Materials* **2022**, *15*, 2858. [CrossRef]
24. Lee, J.; Kim, S.; Lee, K.; Kang, Y. Theoretical Local Buckling Behavior of Thin-Walled UHPC Flanges Subjected to Pure Compressions. *Materials* **2021**, *14*, 2130. [CrossRef]
25. Kozłowski, M.; Galman, I.; Jasiński, R. Finite Element Study on the Shear Capacity of Traditional Joints between Walls Made of AAC Masonry Units. *Materials* **2020**, *13*, 4035. [CrossRef]
26. Wang, L.; Shi, W.; Zhou, Y. Study on self-adjustable variable pendulum tuned mass damper. *Struct. Des. Tall Spéc. Build.* **2018**, *28*, e1561. [CrossRef]
27. Yang, J.; Lu, Z.; Li, P. Large-scale shaking table test on tall buildings with viscous dampers considering pile-soil-structure interaction. *Eng. Struct.* **2020**, *220*, 110960. [CrossRef]
28. Yang, J.; Jing, H.; Li, P. Shaking table test and simulation of 12-story buildings with metallic dampers located on soft soil. *J. Build. Eng.* **2021**, *46*, 103585. [CrossRef]
29. Hernoune, H.; Benabed, B.; Kanellopoulos, A.; Al-Zuhairi, A.H.; Guettala, A. Experimental and Numerical Study of Behaviour of Reinforced Masonry Walls with NSM CFRP Strips Subjected to Combined Loads. *Buildings* **2020**, *10*, 103. [CrossRef]
30. Sun, G.; Li, F.; Zhou, Q. Cyclic Responses of Two-Side-Connected Precast-Reinforced Concrete Infill Panels with Different Slit Types. *Buildings* **2021**, *12*, 16. [CrossRef]
31. Jamšek, A.; Dolšek, M. The Reduced-Degree-of-Freedom Model for Seismic Analysis of Predominantly Plan-Symmetric Reinforced Concrete Wall–Frame Building. *Buildings* **2021**, *11*, 372. [CrossRef]
32. Wang, W.; Quan, C.; Su, S.; Li, Y.; Song, H. Evaluation of seismic performance and effective lateral stiffness for corrugated steel-plate concrete composite structural walls repaired using bottom corner dampers. *Structures* **2022**, *40*, 1–17. [CrossRef]
33. Wen, L.; Cao, W.; Li, Y.; Liu, Y.; Zhou, H. Quantitative study on the influence of foundation valley shape on the behaviour of concrete cut-off walls. *Structures* **2022**, *38*, 861–873. [CrossRef]
34. Naserpour, A.; Fathi, M. Numerical study of demountable shear wall system for multistory precast concrete buildings. *Structures* **2021**, *34*, 700–715. [CrossRef]
35. Grzyb, K.; Jasiński, R. Parameter estimation of a homogeneous macromodel of masonry wall made of autoclaved aerated concrete based on standard tests. *Structures* **2022**, *38*, 385–401. [CrossRef]
36. Nguyen-Van, V.; Nguyen-Xuan, H.; Panda, B.; Tran, P. 3D concrete printing modelling of thin-walled structures. *Structures* **2022**, *39*, 496–511. [CrossRef]
37. Wang, L.; Shi, W.; Zhou, Y. Adaptive-passive tuned mass damper for structural aseismic protection including soil–structure interaction. *Soil Dyn. Earthq. Eng.* **2022**, *158*, 107298. [CrossRef]
38. Drobiec, Ł.; Jasiński, R.; Mazur, W.; Rybraczyk, T. Numerical Verification of Interaction between Masonry with Precast Reinforced Lintel Made of AAC and Reinforced Concrete Confining Elements. *Appl. Sci.* **2020**, *10*, 5446. [CrossRef]
39. Shi, W.; Wang, L.; Lu, Z.; Gao, H. Study on Adaptive-Passive and Semi-Active Eddy Current Tuned Mass Damper with Variable Damping. *Sustainability* **2018**, *10*, 99. [CrossRef]
40. Ye, J.; Jiang, L. Simplified Analytical Model and Shaking Table Test Validation for Seismic Analysis of Mid-Rise Cold-Formed Steel Composite Shear Wall Building. *Sustainability* **2018**, *10*, 3188. [CrossRef]
41. Yang, J.; Li, P.; Yang, Y.; Xu, D. An improved EMD method for modal identification and a combined static-dynamic method for damage detection. *J. Sound Vib.* **2018**, *420*, 242–260. [CrossRef]

42. Yang, J.; Jing, H.; Li, P. Dynamic characteristics and viscous dampers design for pile-soil-structure system. *Struct. Des. Tall Spéc. Build.* **2020**, *29*, e1785. [CrossRef]
43. Jing, H.; Chen, H.; Yang, J.; Li, P. Seismic analysis of steel silo considering granular material-structure interaction. *Structures* **2022**, *37*, 698–708. [CrossRef]
44. Kumar, V.S.; Ganesan, N.; Indira, P.V.; Murali, G.; Vatin, N.I. Flexural Behaviour of Hybrid Fibre-Reinforced Ternary Blend Geopolymer Concrete Beams. *Sustainability* **2022**, *14*, 5954. [CrossRef]
45. Prithiviraj, C.; Saravanan, J.; Kumar, D.R.; Murali, G.; Vatin, N.I.; Swaminathan, P. Assessment of Strength and Durability Properties of Self-Compacting Concrete Comprising Alccofine. *Sustainability* **2022**, *14*, 5895. [CrossRef]
46. Forero, J.A.; Bravo, M.; Pacheco, J.; de Brito, J.; Evangelista, L. Thermal Performance of Concrete with Reactive Magnesium Oxide as an Alternative Binder. *Sustainability* **2022**, *14*, 5885. [CrossRef]
47. Shah, S.K.H.; Uchimura, T.; Kawamoto, K. Permanent Deformation and Breakage Response of Recycled Concrete Aggregates under Cyclic Loading Subject to Moisture Change. *Sustainability* **2022**, *14*, 5427. [CrossRef]
48. Wang, L.; Shi, W.; Zhang, Q.; Zhou, Y. Study on adaptive-passive multiple tuned mass damper with variable mass for a large-span floor structure. *Eng. Struct.* **2019**, *209*, 110010. [CrossRef]
49. Wang, L.; Nagarajaiah, S.; Shi, W.; Zhou, Y. Semi-active control of walking-induced vibrations in bridges using adaptive tuned mass damper considering human-structure-interaction. *Eng. Struct.* **2021**, *244*, 112743. [CrossRef]
50. Shi, W.; Wang, L.; Lu, Z. Study on self-adjustable tuned mass damper with variable mass. *Struct. Control Health Monit.* **2017**, *25*, e2114. [CrossRef]
51. Apay, A.C.; Özgan, E.; Turgay, T.; Akyol, K. Investigation and modelling the effects of water proofing and water repellent admixtures dosage on the permeability and compressive strengths of concrete. *Constr. Build. Mater.* **2016**, *113*, 698–711. [CrossRef]
52. Su, J.; Bloodworth, A. Simulating composite behaviour in SCL tunnels with sprayed waterproofing membrane interface: A state-of-the-art review. *Eng. Struct.* **2019**, *191*, 698–710. [CrossRef]
53. Chuai, J.; Hou, Z.; Wang, Z.; Wang, L. Mechanical Properties of the Vertical Joints of Prefabricated Underground Silo Steel Plate Concrete Wall. *Adv. Civ. Eng.* **2020**, *2020*, 6643811. [CrossRef]
54. Pisova, B.; Hilar, M. Spray-applied waterproofing membranes: Effective solution for safe and durable tunnel linings? *IOP Conf. Ser. Mater. Sci. Eng.* **2017**, *236*, 012087. [CrossRef]
55. *GB/T 193-2003*; Ordinary Thread Diameter and Pitch Series. The General Administration of Quality Supervision, Inspection and Quarantine of the People's Republic of China: Beijing, China, 2003.
56. *GT/T 196-2003*; Ordinary Thread Basic Dimensions. The General Administration of Quality Supervision, Inspection and Quarantine of the People's Republic of China: Beijing, China, 2003.
57. *GB/T 1040-2006*; Plastics Determination of Tensile Properties. The General Administration of Quality Supervision, Inspection and Quarantine of the People's Republic of China: Beijing, China, 2006.
58. *GB 50010-2010*; Design Code for Concrete Structures. The General Administration of Quality Supervision, Inspection and Quarantine of the People's Republic of China: Beijing, China, 2016.